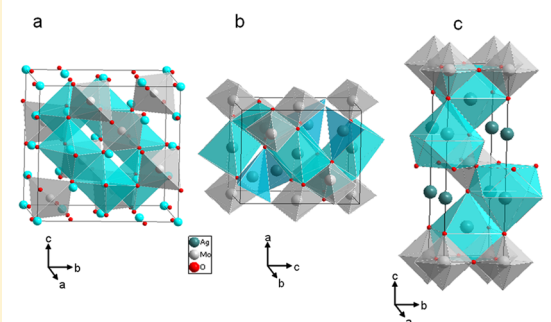


First-Principles Study of Pressure-Induced Phase Transitions and Electronic Properties of Ag_2MoO_4

Armando Beltrán,[†] Lourdes Gracia,^{*,†,‡,§} Elson Longo,^{‡,§} and Juan Andrés[†][†]Departament de Química Física i Analítica, Universitat Jaume I, Campus de Riu Sec, Castelló E-12080, Spain[‡]INCTMN-UNESP, Universidade Estadual Paulista, P.O. Box 355, CEP, Araraquara 14801-907, SP, Brazil[§]INCTMN-UFSCar, Universidade Federal de São Carlos, P.O. Box 676, São Carlos 13565-905, SP, Brazil

ABSTRACT: We have performed a systematic first-principles investigation by using the density functional formalism with the nonlocal B3LYP approximation to calculate structural and electronic properties as well as phase transitions under pressure of silver molybdate, Ag_2MoO_4 . Five phases have been considered: tetragonal Ag_2MoO_4 (with normal and inverse $P4_122$ structures), $\beta\text{-Ag}_2\text{MoO}_4$ (cubic spinel structure), olivine-type (orthorhombic structure), and $\alpha\text{-Ag}_2\text{MoO}_4$ (tetragonal K_2NiF_4 -type structure). Numerical and analytical fittings have been conducted to determine the equilibrium unit cell geometry and equation-of-state parameters for all structures and compounds involved in the phase diagram. Pressure dependencies of band structures, energy gaps, density-of-states (DOS), and vibrational frequencies were investigated. Theoretical results show that the inverse Ag_2MoO_4 with $P4_122$ symmetry is more stable above 15 GPa than the normal spinel structure, while the tetragonal structure is slightly more stable than the cubic representation above 6 GPa due to a tetragonal distortion. We determined the stability against decomposition of Ag_2MoO_4 toward binary oxides (MoO_2 , MoO_3 , Ag_2O , AgO , and Ag_2O_3), metal (Ag and Mo), oxygen, and $\text{Ag}_2\text{Mo}_2\text{O}_7$. Theoretical results point out that $\beta\text{-Ag}_2\text{MoO}_4$ can decompose into $\text{Ag}_2\text{Mo}_2\text{O}_7$ and Ag_2O at 12 GPa.

a) cubic spinel, b-phase, b) inverse tetragonal spinel, c) K_2NiF_4 -type, α -phase

1. INTRODUCTION

The comprehension of materials behavior at high pressure has received much attention in recent decades. Pressure has an important effect on their structure and properties, and advances in techniques and instrumentation have attracted more interest from researchers in solid-state physics, crystal chemistry, geophysics, biology, and materials science, which has resulted in a rich source of new phenomena, including new phases and/or polymorphs. This area represents a prevailing research frontier for fundamental theory and simulation analyses.^{1–7}

The application of high pressure to matter significantly alters the interatomic distances and thus the nature of the intermolecular interactions and the chemical bonding as well as crystal structure and material stability. A sudden change in the arrangement of atoms, such as a structural phase transition associated with a change in crystal symmetry, occurs under applied pressure, and properties of high-pressure phases may be very different from properties under normal conditions. Pressure-dependent phase stability knowledge and the relationship between physical/chemical properties and crystal/electronic structures may facilitate a systematic search for new complex metal oxides. For example, very recently, Maczka et al.⁸ reviewed high-pressure studies of pressure-induced structural phase transitions and amorphization in selected molybdates and tungstates.

Normal and ordered-inverse A_2BO_4 spinel oxides are a family of compounds with a wide range of technological applications.^{9,10} Ag_2MoO_4 belongs to this family and has attracted recent attention due to its chemical stability at elevated temperatures and subsequent high-temperature lubricating properties¹¹ as well as its applications in electrochemical devices and gas sensing,^{11–15} and in surface-enhanced Raman scattering techniques.^{13,16} The morphology and microstructure of Ag_2MoO_4 varied significantly through pH-controlled self-assembly in a simple hydrothermal process, which has produced broomlike or flowerlike structures of $\text{Ag}_2\text{Mo}_2\text{O}_7$ microrods and the formation of microparticles of Ag_2MoO_4 at high pH values.¹⁷ Very recently, a monoclinic $\text{Ag}_2\text{Mo}_2\text{O}_7$ nanowire has been synthesized as a new Ag–Mo–O nanophotocatalyst material.¹⁸

The crystal structure of Ag_2MoO_4 was obtained by Wyckoff.¹⁹ Computational and experimental studies of Ag_2MoO_4 show that its layered atomic structure facilitates sliding and suggests that the single phase almost instantly segregates into a binary system, which consists of silver clusters and molybdenum oxide at temperatures near the melting point.²⁰ Ag_2MoO_4 can be found in two forms: $\alpha\text{-Ag}_2\text{MoO}_4$ has

Received: December 2, 2013

Revised: January 19, 2014

Published: January 22, 2014

a tetragonal structure, while β -Ag₂MoO₄ is cubic with a spinel structure. The α -phase irreversibly transforms to the β -phase upon heating above ambient temperature.

First-principles calculations are a powerful complement to experimental techniques and provide detailed structural information to understand phenomena such as pressure-induced phase transition and electronic properties at the atomic level. In this context, we previously studied the effect of pressure on the MgAl₂O₄ normal spinel as well as the Zn₂SnO₄ inverse spinel structure.^{21,22} The motivation for our investigation essentially arises from the results of a recent work concerning the behavior of the cubic spinel phase of Ag₂MoO₄ at high pressure as characterized by X-ray diffraction (XRD) and Raman spectroscopy.²³ The XRD technique reveals the averaged structure of the long-range scale of materials, while Raman spectroscopy provides a sensitive probe for structural distortion, short-range ordering, and symmetry of a solid. A computational study based on first principles was performed to further understand these observed experimental results. In this study, we investigate structural and electronic properties of Ag₂MoO₄ under high-pressure conditions in the framework of density functional theory (DFT) by the nonlocal B3LYP approximation. Possible phase transformations have been explored by analyzing respective equations-of-state (EOS) parameters and by obtaining the corresponding bulk modulus and transition pressures. Electronic structures, including DOS and band structures, were calculated on the basis of optimized geometries. In addition, energetic aspects of different dissociation channels to obtain binary and complex metal oxides, metals, and oxygen were analyzed.

The paper is organized as follows: section 2 describes computational details, and section 3 contains theoretical results together with a discussion concerning the local compressibility and phase stability as well as the electronic structure analysis for the different phases. In addition, vibrational properties derived from calculations are discussed in detail and compared with experimental values. Standard Gibbs free energies of possible dissociation processes at ambient temperature and pressure are also analyzed in this section. Finally, we summarize our main conclusions in section 4.

2. THEORETICAL CALCULATIONS

First-principles total-energy calculations were carried out within the periodic DFT framework by use of the CRYSTAL09 program package.²⁴ Becke's three-parameter hybrid nonlocal exchange functional²⁵ combined with the Lee–Yang–Parr gradient-corrected correlation functional, B3LYP,²⁶ was used. Ag, Mo, and O centers have been described in the schemes [HAYWSC]-311(d31)G, [HAYWSC]-311(d31)G, and 6-31G*, respectively, where [HAYWSC] stands for the Hay and White nonrelativistic small-core pseudopotential.

Diagonalization of the Fock matrix was performed at adequate *k*-point grids in the reciprocal space, which depends on the phase under treatment using Pack–Monkhorst/Gilat shrinking factors: IS = ISP = 4. The use of a different number of *k*-points is because the primitive unit cells of different phases contain different numbers of atoms. Thresholds controlling the accuracy of the calculation of Coulomb and exchange integrals were set to 10^{−8} (ITOL1–ITOL4) and 10^{−14} (ITOL5), which ensures a convergence in total energy better than 10^{−7} hartree in all cases, whereas the percent of Fock/Kohn–Sham matrices mixing was set to 40 (IPMIX = 40).²⁴

The vibrational-frequencies calculation in CRYSTAL is performed at the Γ point within the harmonic approximation, and the dynamic matrix is computed by the numerical evaluation of the first derivative of analytical atomic gradients. The calculation of the Hessian matrix in the vibrational-frequencies module in CRYSTAL permits access to the entropy and consequently to an estimation of the standard Gibbs free energy at ambient temperatures.

To consider the effect of pressure on this system, we optimized geometrical parameters and internal positions of all phases, at a number of fixed external pressures (EXTPRESS option), ranging from ambient pressure to 50 GPa. Fittings of the computed (*E*, *V*) data provide pressure bulk modulus zero values and its pressure derivative as well as free energy–pressure curves for the five polymorphs studied.²⁷

Four types of decomposition channels have been studied, and the corresponding Gibbs decomposition free energy, $\Delta_d G^0$, at ambient temperature is calculated by use of the following equations:

(i) Formation of metal oxides

$$\Delta_d G^0 = \sum_i^{\text{metal oxides}} G_i^0 - G_{\text{Ag}_2\text{MoO}_4}^0$$

(ii) Formation of metal and metal oxides

$$\Delta_d G^0 = \sum_i^{\text{metals + metal oxides}} G_i^0 - G_{\text{Ag}_2\text{MoO}_4}^0$$

(iii) Formation of metal oxides, metals, and oxygen

$$\Delta_d G^0 = \sum_i^{\text{metals + metal oxides}} G_i^0 + \mu_{\text{O}_2}^0(T) - G_{\text{Ag}_2\text{MoO}_4}^0$$

(iv) Formation of metals and oxygen

$$\Delta_d G^0 = \sum_i^{\text{metals}} G_i^0 + \mu_{\text{O}_2}^0(T) - G_{\text{Ag}_2\text{MoO}_4}^0$$

where

$$G_i^0 = [E_{\text{EL}}^{\text{P}} + E_0^{\text{P}} + E_{\text{vib}}^{\text{P}}(T) + pV_{\text{vib}}^{\text{P}} - TS_{\text{vib}}^{\text{P}}]$$

Here, E_{EL}^{P} is the total electronic energy, E_0^{P} is the zero-point energy, $E_{\text{vib}}^{\text{P}}$ is the thermal contribution to the vibrational energy, and $S_{\text{vib}}^{\text{P}}$ is the vibrational entropy. For both metal oxides and single metals, the most stable solid polymorphs at ambient pressure and temperature are considered in our calculations. All geometric parameters are optimized, and for the optimized structures, their vibrational properties were calculated.

When O₂(g) is a product of the dissociation channel, we employ the following equation within an ideal gas model to calculate the standard chemical potential, $\mu_{\text{O}_2}^0(T)$, of the O₂ molecule:

$$\mu_{\text{O}_2}^0(T) = E_{\text{EL}}^{\text{O}_2} + E_0^{\text{O}_2} + E^{\text{O}_2} + \kappa_{\text{B}}T - TS^{\text{O}_2}$$

The thermal energy E^{O_2} and entropy S^{O_2} include the translational, rotational, and vibrational contributions to the chemical potential of O₂. This strategy is used to minimize errors due to incorrect estimation of the O₂ binding energy, which is significantly overestimated by 1–1.5 eV when the standard DFT functional is used.^{28–30} Ways to circumvent this

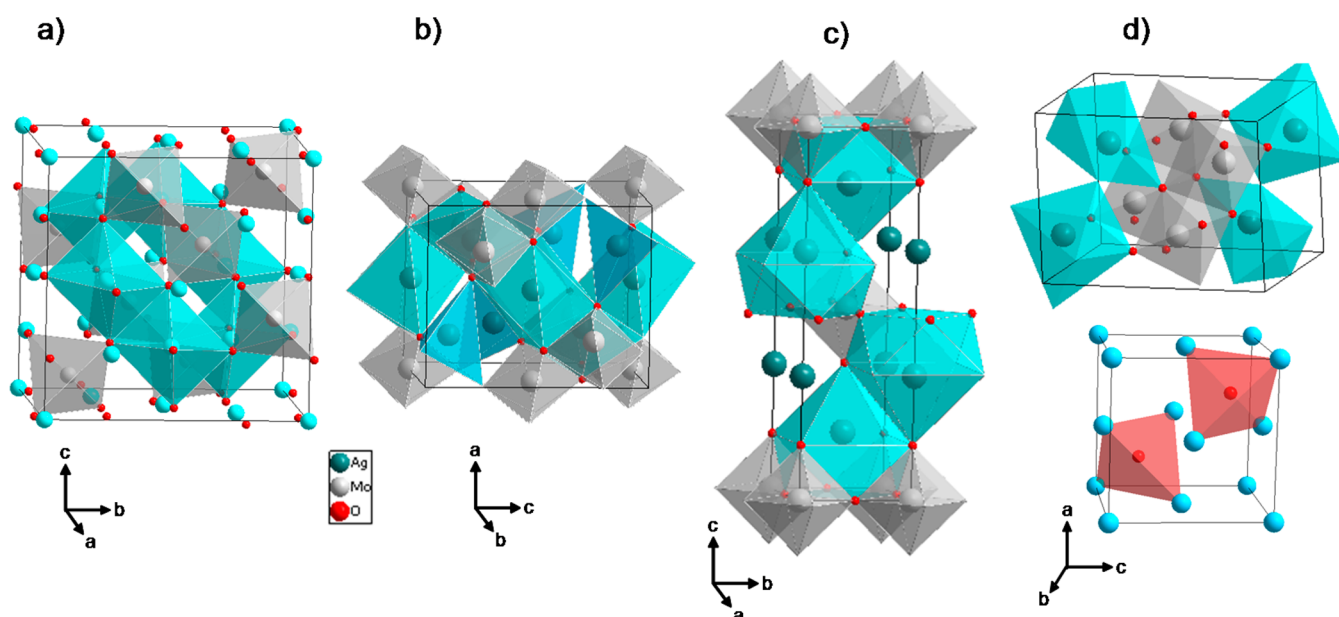


Figure 1. Polyhedral representation of unit cells: (a) cubic spinel (β) ($Fd\bar{3}mZ$), (b) inverse tetragonal spinel ($P4_122$), (c) K_2NiF_4 -type structure (α - Ag_2MoO_4Z), and (d) monoclinic $Ag_2Mo_2O_7$ ($P2_1/c$) and Ag_2O ($Pn\bar{3}m$) structures.

Table 1. Unit Cell a Parameter and Metal–Oxygen Distances at Different Pressures and Bulk Modulus B_0 and Its Pressure Derivative B_0' for the $Fd\bar{3}m$ Space Group

P (GPa)	a (Å)	$u(O)$	$d(Ag-O) \times 6$ (Å)	$d(Mo-O) \times 4$ (Å)	B_0 (GPa)	B_0'
Experimental ²³						
ambient	9.3127				124	1.5 ± 1.3
					113	4 (fixed)
					109	5 (fixed)
2.3	9.264	0.2318				
Calculated						
ambient	9.4274	0.2345	2.5115	1.7880	86.8	5.7
					103.6	4 (fixed)
5	9.2714	0.2359	2.4551	1.7816		
10	9.1508	0.2370	2.4121	1.7759		
15	9.0516	0.2379	2.3771	1.7706		
20	8.96662	0.2387	2.3475	1.7657		
25	8.8924	0.2393	2.3219	1.7609		
30	8.8264	0.2399	2.2993	1.7564		
35	8.7672	0.2404	2.2791	1.7523		
40	8.7133	0.2408	2.2610	1.7482		
45	8.6637	0.2412	2.2445	1.7441		
50	8.6179	0.2416	2.2294	1.7402		

problem have been developed, for example, employing a water reference instead of a molecular oxygen-based reference.³¹ However, the method used in this study correctly reproduces the experimental data.

3. RESULTS AND DISCUSSION

3.1. Structural Properties. β - Ag_2MoO_4 belongs to the spinel structure with space group $Fd\bar{3}m$, which is similar to $MgAl_2O_4$; this phase diagram has been studied extensively both experimentally³² and theoretically.^{21,22} Figure 1a shows that the conventional cubic unit cell contains eight formula units. Mo ions (gray in the figure) occupy tetrahedral 8a sites, while Ag ions (blue in the figure) reside at the octahedral 16d position. Oxygen atoms (red in the figure) stay at 32e positions. Arora et al.²³ performed powder XRD measurements at ambient pressure; the results show a single-phase material with a lattice

parameter of 9.313 Å. The calculated lattice parameter, oxygen internal coordinates, and distances between the metal ions and the oxygen at different pressures, as well as the bulk modulus and its pressure derivative, for this β - Ag_2MoO_4 structure are listed in Table 1.

Our calculations at ambient pressure yield a lattice parameter of 9.427 Å, which is only 1.2% greater than the experimental value.²³ Calculated P – V – E data are fitted by use of a third-order Birch–Murnaghan (BM) EOS to obtain the ambient pressure bulk modulus B_0 and its pressure derivative B_0' .²³ At ambient pressure we obtain a bulk modulus of 86.7 GPa and a B_0' of 5.7. When a fixed value for B_0' of 4 was used, the fitting yields a B_0 value of 103.6 GPa. This result compares well with experimental data obtained by Arora et al.:²³ 113 GPa for B_0 at B_0' fixed to 4.

Table 1 lists lattice parameters as well as Ag–O and Mo–O distances, which decrease monotonically as a function of pressure; the AgO_6 unit is much more compressible than the MoO_4 unit. We calculated the bond compressibility, k , defined as $[1/d(\text{MeO})][\partial d(\text{MeO})/\partial P]$, where $d(\text{MeO})$ are the metal–oxygen distances from the values in Table 1. The Mo–O bond is less compressible than the Ag–O bond; on the other hand, we find two regions of different bond compressibilities, the first between 0 and 6 GPa and the second from 6 up to 50 GPa. Compressibilities for the Mo–O bond are $7.27 \times 10^{-4} \text{ GPa}^{-1}$ from 0 to 6 GPa and $5.03 \times 10^{-4} \text{ GPa}^{-1}$ from 10 to 50 GPa, whereas for the Ag–O bond their corresponding values are $4.38 \times 10^{-3} \text{ GPa}^{-1}$ and $1.99 \times 10^{-3} \text{ GPa}^{-1}$, respectively.

On the basis of the ratio between A and B cation radii³³ (r_A/r_B), we have also studied orthorhombic structures: Sr_2PbO_4 -type (olivine), CaFe_2O_4 -type, and tetragonal K_2NiF_4 -type (α - Ag_2MoO_4 structure). After corresponding tests, we chose olivine and K_2NiF_4 types as possible polymorphs; we performed both structure calculations at different pressures ranging from ambient pressure to 50 GPa.

Figure 1c shows the unit cell of the tetragonal K_2NiF_4 -type structure of α - Ag_2MoO_4 . In this structure, Mo atoms occupy 2(a) Wyckoff positions (0, 0, 0) at the center of a distorted octahedron (gray in the figure), whereas Ag atoms are located at the 4(e) Wyckoff positions (0, 0, z) and show 9-fold coordination with three (1 + 4 + 4) different Ag–O distances (blue in the figure).

Crystal structures of A_2BO_4 spinel oxides can possess different distributions of A and B cations over tetrahedrally and octahedrally coordinated sites. In the normal structure described above, the Oh sites were occupied exclusively by A cations and the Td sites by B cations, whereas inverse spinel has half the A cations occupying Td sites and the other half of A together with all of the B atoms populating the Oh sites, which is similar to a 50%–50% binary alloy on Oh sites. Therefore, as reported by Stevanovic et al.,³⁴ inverse spinel corresponds to a class of configurations rather than a single crystallographic structure.

Normal and ordered-inverse structures can also undergo characteristic structural changes as a function of temperature,^{35,36} which is a consequence of A and B cations exchanging their lattice sites. Both normal and inverse spinel structure can be described within the tetragonal $P4_122$ space group since they possess two octahedral and one tetrahedral site, at 4a (0, y , 0), 4b ($1/2$, y , 0), and 4c (x , x , $3/8$) Wyckoff positions, respectively, whereas oxygen atoms occupy two different 8d (x , y , z) positions.

We have optimized these normal and inverse Ag_2MoO_4 structures at different pressures up to 50 GPa. Table 2 lists geometric parameters for these two orderings at ambient pressure.

Total energy calculations as a function of volume, as well as the variation of Gibbs free energy at ambient temperature, ΔG , as a function of pressure, for the cubic spinel (β), K_2NiF_4 -type (α) and tetragonal normal and inverse spinel calculated structures are depicted in Figure 2a. ΔG – P values of the normal tetragonal structure superimpose almost perfectly with those values that correspond to the cubic spinel structure below 6 GPa. Thus, both (α and β) curves cross at high pressure. The K_2NiF_4 -type phase becomes more stable than the spinel at pressures above 32 GPa (see Figure 2b). Our calculations also indicate that olivine is the most stable structure of Ag_2MoO_4

Table 2. Optimized Structure for Normal and Inverse Tetragonal Ag_2MoO_4 Structures at Ambient Pressure

	site	x	y	z
Normal: $a = 6.6735 \text{ \AA}$, $c = 9.4041 \text{ \AA}$, $V = 418.82 \text{ \AA}^3$				
Ag	4a	0	0.2503	0
Ag	4b	0.5	0.2501	0
Mo	4c	0.2501	0.2501	0.375
O	8d	0.0314	0.2499	0.2650
O	8d	0.4683	0.2499	0.2649
Inverse: $a = 6.6476 \text{ \AA}$, $c = 8.5547 \text{ \AA}$, $V = 412.93 \text{ \AA}^3$				
Ag	4b	0.5	0.2609	0
Ag	4c	0.2525	0.2525	0.375
Mo	4a	0	0.2531	0
O	8d	−0.4193	0.1966	0.2815
O	8d	−0.1948	0.2008	0.2210

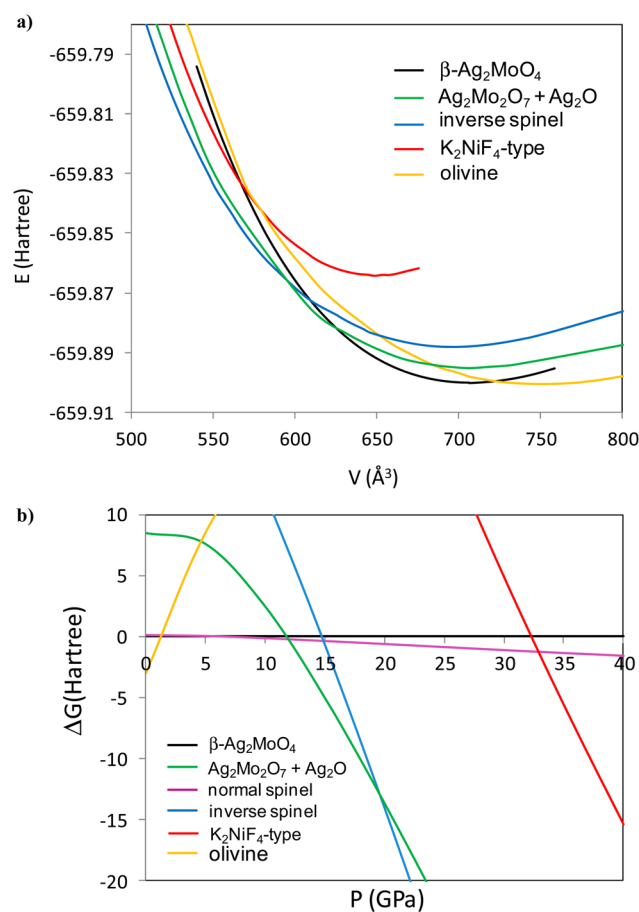


Figure 2. (a) Total energy versus volume and (b) variation in free Gibbs energy vs pressure (with the β structure as a reference) for tetragonal Ag_2MoO_4 (with normal and inverse $P4_122$ structures), β - Ag_2MoO_4 (spinel structure), olivine-type (orthorhombic structure), and α - Ag_2MoO_4 (tetragonal K_2NiF_4 -type structure) and the sum of $\text{Ag}_2\text{Mo}_2\text{O}_7$ and Ag_2O .

below 1 GPa. After corresponding vibrational calculations, we find that neither olivine nor K_2NiF_4 -type structures correspond to the high-pressure tetragonal phase that Arora et al.²³ suggest coexists with the cubic phase over a range of pressures (from 2.3 to 12 GPa).

The phase diagram for silver and molybdenum oxides (MoO_3 – Ag_2O) and their reactions were studied by Wenda.^{37,38} Here, to obtain energetics for the Ag_2MoO_4 decomposition

process into their constituent oxides, metals, and oxygen as well as to $\text{Ag}_2\text{Mo}_2\text{O}_7$, we calculated structures of MoO_2 , MoO_3 , Ag_2O , AgO , Ag_2O_3 , Ag , Mo , and $\text{Ag}_2\text{Mo}_2\text{O}_7$, initially at ambient pressure, and for favorable cases at different pressures ranging from ambient pressure to 50 GPa. Table 3 illustrates the

Table 3. Calculated Values of $\Delta_d G^0$ and ΔV for Different Dissociation Channels of Ag_2MoO_4 toward Binary Oxides, Metals, Oxygen, and $\text{Ag}_2\text{Mo}_2\text{O}_7$ ^a

dissociation channel	$\Delta_d G^0$ (eV)	ΔV (\AA^3)
$\text{Ag}_2\text{MoO}_4 \rightarrow \text{Ag}_2\text{O} + \text{MoO}_3$	0.76	+2.69
$\text{Ag}_2\text{MoO}_4 \rightarrow \text{Ag} + \text{AgO} + \text{MoO}_3$	2.39	−16.93
$2\text{Ag}_2\text{MoO}_4 \rightarrow \text{Ag}_2\text{O}_3 + \text{Ag}_2\text{O} + 2\text{MoO}_2$	6.61	−18.67
$2\text{Ag}_2\text{MoO}_4 \rightarrow 4\text{AgO} + 2\text{MoO}_2$	5.93	−5.23
$3\text{Ag}_2\text{MoO}_4 \rightarrow 2\text{Ag}_2\text{O}_3 + 2\text{AgO} + \text{Mo} + 2\text{MoO}_2$	19.11	−42.74
$\text{Ag}_2\text{MoO}_4 \rightarrow \text{MoO}_3 + 2\text{Ag} + \frac{1}{2}\text{O}_2$	2.46	
$\text{Ag}_2\text{MoO}_4 \rightarrow \text{Ag}_2\text{O} + \text{Mo} + \frac{3}{2}\text{O}_2$	7.11	
$\text{Ag}_2\text{MoO}_4 \rightarrow 2\text{Ag} + \text{Mo} + 2\text{O}_2$	8.81	
$2\text{Ag}_2\text{MoO}_4 \rightarrow \text{Ag}_2\text{Mo}_2\text{O}_7 + \text{Ag}_2\text{O}$	0.27	−0.12
$2\text{Ag}_2\text{MoO}_4 \rightarrow \text{Ag}_2\text{Mo}_2\text{O}_7 + \text{AgO} + \text{Ag}$	1.90	−19.74

^a $\Delta_d G^0$ = free energy of dissociation; ΔV = volume variation. Binary oxides are MoO_2 , MoO_3 , Ag_2O , AgO , and Ag_2O_3 ; metals are Ag and Mo .

variation of free Gibbs energy and the volume variation at ambient pressure for the investigated dissociation channels. An analysis of the results shows that all channels have ΔG positive values, and ΔV negative values: however, the decomposition of $\beta\text{-Ag}_2\text{MoO}_4$ into Ag_2O and $\text{Ag}_2\text{Mo}_2\text{O}_7$ ($2\text{Ag}_2\text{MoO}_4 \rightarrow \text{Ag}_2\text{Mo}_2\text{O}_7 + \text{Ag}_2\text{O}$) has a slightly negative value (−0.12 \AA^3) for the total volume variation along the process and the lowest free energy barrier (0.27 eV) of all the investigated decomposition channels. Therefore, we studied this process in more detail.

Figure 1d shows that the monoclinic $\text{Ag}_2\text{Mo}_2\text{O}_7$ structure consists of infinite chains formed by blocks of four edge-shared MoO_6 octahedra (in gray) joined by edge-sharing with silver ions situated between chains. The fitting of normal tetragonal data to the BM EOS yields $B_0 = 85.7$ GPa ($B_0' = 5.7$), which are close to previous values obtained for the cubic spinel ($\beta\text{-Ag}_2\text{MoO}_4$), $B_0 = 86.8$ GPa ($B_0' = 5.7$); for the inverse tetragonal structure, we obtained $B_0 = 59.8$ GPa ($B_0' = 6.1$). If we fix B_0' to 4, the corresponding B_0 values are 103.6, 101.1, and 74.0 for cubic, normal and inverse tetragonal structures, respectively. Figure 2b shows that the inverse tetragonal structure is more stable above 15 GPa than the normal spinel. Our calculations show that, above 6 GPa, a tetragonal distortion gives normal tetragonal structures slightly more stable than their cubic representation, which will be discussed in depth after Raman results are shown. Figure 2b also shows that at 12 GPa the sum of the silver oxide and the silver dimolybdate has a lower free energy than the $\beta\text{-Ag}_2\text{MoO}_4$, but above 18 GPa the inverse tetragonal structure becomes the most stable.

3.2. Electronic Properties. The effect of pressure on band structures of all investigated Ag_2MoO_4 polymorphs has also been examined. At ambient pressure, calculated band structures along adequate symmetry lines of cubic, tetragonal, and

orthorhombic Bravais lattices show that $\beta\text{-Ag}_2\text{MoO}_4$ has a band gap of 4.19 eV with an indirect transition from the valence band (VB) Γ point to the X point of the conduction band (CB), with a direct band gap at Γ of 4.40 eV; the inverse spinel structure has an indirect band gap of 3.01 eV from M to Γ (with a direct gap at Γ of 3.18 eV); K_2NiF_4 -type (α) Ag_2MoO_4 has an indirect gap from N to Γ of only 0.62 eV and the corresponding direct gap at Γ is 0.85 eV.

Figure 3 shows the band structure and DOS projected on atoms and orbitals for $\beta\text{-Ag}_2\text{MoO}_4$ at ambient pressure and for the tetragonal inverse spinel at 15 GPa. In $\beta\text{-Ag}_2\text{MoO}_4$ the bottom of the VB is mainly formed by hybridization between Ag 4d and O 2p orbitals, while CB is mainly formed by hybridization between Mo 4d and O 2p orbitals. For both transition metals $d_{x^2-y^2}$ and d_{z^2} states produce the major contribution. At 15 GPa, indirect and direct band gaps of $\beta\text{-Ag}_2\text{MoO}_4$ are 3.92 and 3.94 eV, respectively. However, the inverse spinel structure band gap is direct at Γ and equal to 2.72 eV. An analysis of the projected DOS in Figure 3b shows that the VB maximum is derived mostly from O 2p and Ag d_{z^2} orbitals with a minor contribution from d_{xy} . The minimum CB is formed basically by Mo $d_{x^2-y^2}$ and d_{xz} .

Recently Li et al.³⁹ synthesized cube-like microstructures of Ag_2MoO_4 and from their optical measurements deduced a band gap of 3.37 eV.

$\text{Ag}_2\text{Mo}_2\text{O}_7$ at ambient pressure has a direct gap at the D ($-1/2, 0, 1/2$) point of 3.67 eV (the corresponding direct gap at Γ is equal to 4.13 eV) whereas at 12 GPa a direct gap is displayed at E ($1/2, 1/2, 1/2$) of 3.24 eV, and a direct gap is displayed at Γ of 3.66 eV. Figure 4 shows the band structure and DOS projected on atoms and orbitals for $\text{Ag}_2\text{Mo}_2\text{O}_7$ at the pressure transition (12 GPa). An analysis of the projected DOS in Figure 4 shows that the VB maximum is composed mostly from O 2p and Ag d_{xz} orbitals. The CB minimum is derived basically from Mo d_{xy} and d_{xz} .

Recently a higher photocatalytic activity reported for $\text{Ag}_2\text{Mo}_2\text{O}_7$ was mainly attributed to the smaller band gap of 2.65 eV.⁴⁰ From the UV–vis reflectivity spectrum, the optical band gap of $\text{Ag}_2\text{Mo}_2\text{O}_7$ nanowires is reported to be 2.94 eV, and the luminescence in the visible region is explained by DFT calculations with consideration of oxygen vacancies.⁴¹

3.3. Vibrational Properties. Lattice vibrations are crucial for materials modeling, and their behavior under pressure provides useful information regarding structural instabilities and phase transformations. The spinel structure primitive cell contains two Ag_2MoO_4 units that provide a total of 42 vibrational degrees of freedom. Group theoretical considerations lead for the spinel structure to five Raman-active modes:⁴²

$$\Gamma = A_{1g} + E_g + 3T_{2g}$$

Frequencies (ω) of Raman-active modes for the $\beta\text{-Ag}_2\text{MoO}_4$ structure have been calculated as well as Grüneisen parameters ($\gamma = B_0 \partial \ln \omega / \partial P$) from its pressure dependencies. Figure 5 shows corresponding frequency shifts for Raman-active modes as a function of pressure. Table 4 lists calculated pressure coefficients for all modes and their Grüneisen parameters which were calculated with the value of $B_0 = 103.6$ GPa reported in this study.

The A_{1g} mode at 895 cm^{-1} corresponds to the Mo–O bond symmetric stretching vibration of the MoO_4 unit, whereas the T_{2g} mode at 790 cm^{-1} represents asymmetric stretching; both modes have large pressure dependencies. The T_{2g} mode we

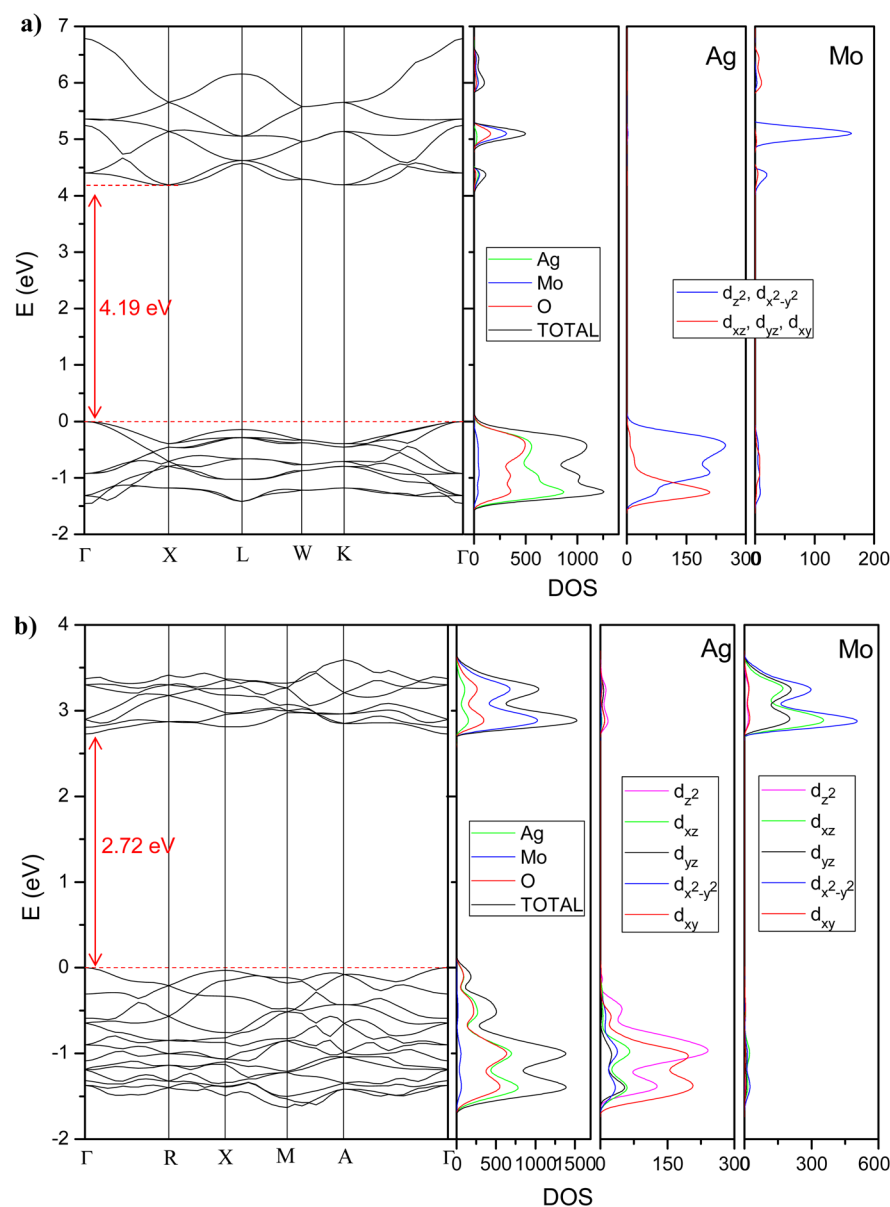


Figure 3. Band structure and DOS projected on atoms and orbitals for (a) β - Ag_2MoO_4 cubic structure at 0 GPa and (b) tetragonal $\text{Ag}_2\text{MoO}_4\text{Z}$ with inverse $P4_122$ symmetry structure at 15 GPa.

found at 367 cm^{-1} corresponds to the bending mode of the MoO_4 unit. The E_g mode at 279 cm^{-1} is a lattice mode involving vibrations of Ag cations. The T_{2g} mode at 89 cm^{-1} also involves Ag cations but has not been experimentally detected. Large pressure coefficients of stretching internal modes for MoO_4 units suggest that their pressure dependence is strong, so a little distance variation for Mo–O bonds can lead to a great frequency variation according to their low bond compressibility (see above). On the other hand, although AgO_6 units present high compressibility, the low value of the pressure coefficient for the E_g lattice mode implies that vibrations involving Ag cations are less sensitive to pressure.

Arora et al.²³ reported that as pressure is increased, intensities of the modes associated with the cubic phase are reduced while new modes appear with increased intensities as a function of pressure. The modes they found at 841 and 921 cm^{-1} were considered to arise from the splitting of the 873

cm^{-1} mode of the cubic phase due to the lowering of symmetry across the cubic–tetragonal transition.

The primitive cell of the tetragonal ($P4_122$) structure contains four Ag_2MoO_4 units, which results in a total of 84 vibrational degrees of freedom, twice the degrees of the cubic spinel structure. Group theoretical considerations⁴² for this structure reveal 36 Raman-active modes:

$$\Gamma = 6A_1 + 7B_1 + 8B_2 + 15E_g$$

For the inverse tetragonal structure, there are three Raman-active modes around or above 800 cm^{-1} . Table 5 lists these calculated frequencies (cm^{-1}) at different pressures, as well as their pressure coefficients and Grüneisen parameters (γ).

B_1 and E modes involve stretching of Mo–O bonds and bending of Mo–O–Ag angles. The A_1 mode reveals curious behavior: from 0 to 6 GPa, this mode involves stretching of Mo–O bonds and bending of Mo–O–Ag angles, whereas above 10 GPa, only stretching of Mo–O bonds of MoO_6

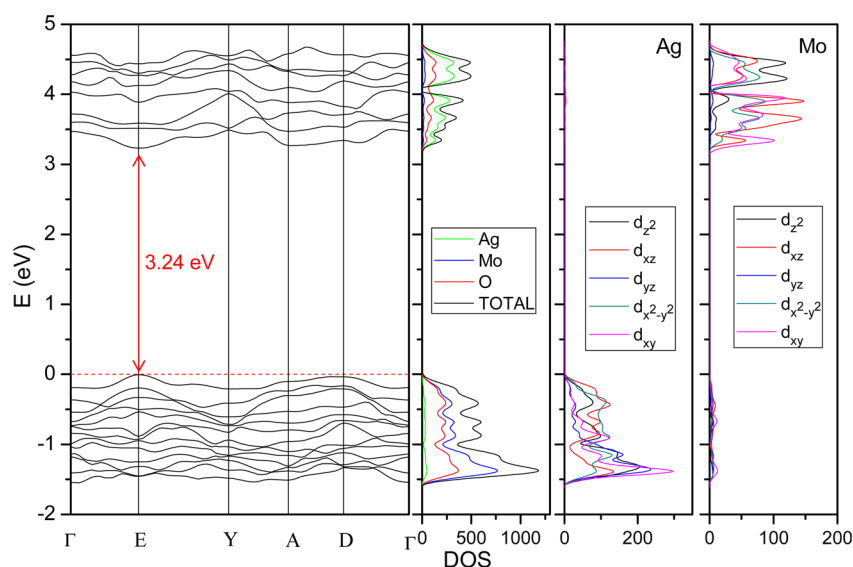


Figure 4. Band structure and DOS projected on atoms and orbitals for $\text{Ag}_2\text{Mo}_2\text{O}_7$ at 12 GPa.

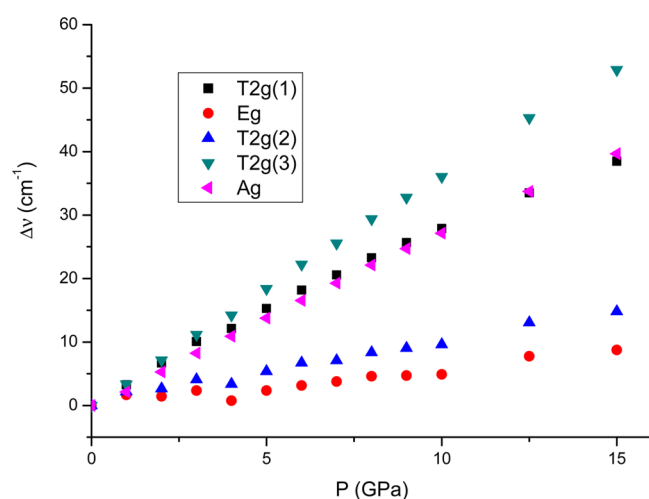


Figure 5. Shift of Raman modes with respect to the corresponding frequency at ambient pressure for $\beta\text{-Ag}_2\text{MoO}_4$ as a function of pressure.

Table 4. Pressure Coefficients and Grüneisen Parameters of Raman-Active Modes^a

mode	frequency (cm ⁻¹)	P coefficient (cm ⁻¹ /GPa)	Grüneisen parameter (□)
T _{2g} (1)	89	1.59	1.85
E _g	279 [278] (272)	0.77 [0.24]	0.29 [0.10]
T _{2g} (2)	367 [352] (348)	0.99 [1.50]	0.23 [0.48]
T _{2g} (3)	790 [761] (756)	3.13 [4.08]	0.41 [0.61]
A _{1g}	895 [873] (870)	2.31 [2.10]	0.27 [0.27]

^aExperimental values from ref 23 are given in brackets and those from ref 16 are given in parentheses.

distorted octahedra are involved. For the A₁ mode, a pressure coefficient of 1.58 cm⁻¹/GPa was obtained, which is similar to the 1.69 cm⁻¹/GPa value for the 841 cm⁻¹ mode reported by Arora et al.²³ above 6 GPa that they associate with a tetragonal structure.

When we consider the normal tetragonal structure, we find a total of five Raman-active modes above 800 cm⁻¹. In Table 6 we show these calculated frequencies (cm⁻¹) at different

Table 5. Calculated Frequencies up to 800 cm⁻¹, Pressure Coefficients, and Grüneisen Parameters (γ) for Inverse Tetragonal Structure

P (GPa)	B ₁	E	A ₁
ambient	790	804	817
2	795	807	820
4	799	810	822
6	803	813	825
10	811	821	832
12.5	815	823	834
15	820	829	841
17.5	824	830	843
20	828	833	846
25	837	842	856
30	845	849	864
P coefficient (cm ⁻¹ /GPa)	1.84	1.51	1.56
γ	0.17	0.14	0.14

pressures, as well as their pressure coefficients and Grüneisen parameters (γ).

All five vibrations correspond to stretching modes of the MoO₄ unit. The A₁ mode also displays different behavior below and above 6 GPa; below 6 GPa it corresponds to symmetric stretching of Mo–O bonds of MoO₄ units, whereas at 10 GPa and above, it involves stretching of Mo–O bonds and bending of the Mo–O–Ag angles. This A₁ mode has a frequency similar to the A_{1g} mode of the cubic spinel. If the normal structure coexists with the inverse, this A₁ mode could correspond to the 921 cm⁻¹ mode reported by Arora et al.,²³ although its pressure coefficient is closer to the corresponding experimental cubic 873 cm⁻¹ mode than to the tetragonal 921 cm⁻¹ mode. On the other hand, the presence of more frequencies can explain the broadening of signals in Raman spectra.

On the basis of previous results, we propose the following sequence of stability as a function of pressure increase: olivine → (P ≥ 1 GPa) cubic spinel (β-Ag₂MoO₄) → (6 GPa < P < 15 GPa) tetragonal normal structure → (P ≥ 15 GPa) inverse tetragonal structure.

Table 6. Calculated Frequencies up to 800 cm^{-1} , Pressure Coefficients, and Grüneisen Parameters (γ) for Normal Tetragonal Structure

P	E	B ₁	E	E	A ₁
ambient	811	819	869	887	896
2	820	827	878	894	903
4	828	835	885	900	908
6	836	842	893	906	914
10	850	856	906	916	925
12.5	859	865	915	923	931
15	868	873	922	929	937
17.5	876	881	930	936	943
20	884	889	937	942	949
25	900	904	950	955	963
30	915	919	962	968	974
P coefficient ($\text{cm}^{-1}/\text{GPa}$)	3.45	3.33	3.10	2.67	2.60
γ	0.43	0.41	0.36	0.30	0.29

4. CONCLUSIONS

This study is part of a large theoretical effort to access crystal structures under pressure, in particular, the physical/chemical spinel-based compounds. The reported calculations provide new structural and electronic results from first-principles calculations.

Ground-state properties and high-pressure behavior of Ag_2MoO_4 were studied by first-principles calculations within the framework of DFT. These results provide deeper insight into the relative stability and structural, electronic, and vibrational properties of different phases.

On the basis of quantum chemical simulations, we provide the Ag_2MoO_4 decomposition to MoO_3 and Ag_2O mixture and to $\text{Ag}_2\text{Mo}_2\text{O}_7$ and Ag_2O , as well as toward MoO_3 , AgO , and Ag structures. Structural, electronic, and vibrational properties have been characterized for different bulk phases as well as their response to hydrostatic pressure. The main results can be summarized as follows:

(i) The bulk modulus was calculated by fitting pressure–volume–energy data to the second-order Birch–Murnaghan EOS, and its pressure derivative at corresponding equilibrium phases; calculated geometrical, vibrational, and electronic ground-state properties for $\beta\text{-Ag}_2\text{MoO}_4$ are in good agreement with experimental data and other theoretical results.

(ii) Theoretical results show that $\beta\text{-Ag}_2\text{MoO}_4$ structural material can undergo chemical changes to form $\text{Ag}_2\text{Mo}_2\text{O}_7$ and Ag_2O structures at 12 GPa, while the decomposition of $\beta\text{-Ag}_2\text{MoO}_4$ in MoO_3 and Ag_2O oxides is not energetically feasible.

(iii) We demonstrate that $\beta\text{-Ag}_2\text{MoO}_4$ has an indirect band gap of 4.19 eV from Γ to the X point [bottom of the VB and top of the CB, formed mainly by hybridization between Ag 4d and Mo 4d ($d_{x^2-y^2}$ and d_{z^2}) orbitals with O 2p orbitals, respectively].

(iv) The band gap of the inverse spinel structure at 15 GPa is direct at Γ and equal to 2.72 eV; the VB maximum derived mostly from O 2p and Ag d_{z^2} orbitals, and the CB minimum was basically formed by Mo $d_{x^2-y^2}$ and d_{xz} orbitals.

(v) The $\text{Ag}_2\text{Mo}_2\text{O}_7$ structure at 12 GPa shows a direct gap at $E(1/2, 1/2, 1/2)$ of 3.24 eV; the VB maximum was composed mostly from O 2p and Ag d_{xz} orbitals, and the CB minimum was derived basically from Mo d_{xy} and d_{xz} orbitals.

(vi) Vibrational frequency values as well as their pressure dependence for $\beta\text{-Ag}_2\text{MoO}_4$ and tetragonal normal and inverse Ag_2MoO_4 structures were obtained.

We hope that this comprehensive study serves as a guideline for the interpretation of various experiments involving different phases of the Ag_2MoO_4 system and on related complex oxides, as well as for the interpretation of results reported in this study.

AUTHOR INFORMATION

Corresponding Author

*E-mail lgracia@uji.es.

Notes

The authors declare no competing financial interest.

ACKNOWLEDGMENTS

We acknowledge Generalitat Valenciana (Prometeo/2009/053 project), Ministerio de Ciencia e Innovación (CTQ2009-14541-C02) Programa de Cooperación Científica con Iberoamerica (Brazil), and Ministerio de Educación, Cultura y Deporte (PHB2009-0065 project). This work is also supported by Spanish MALTA-Consolider Ingenio 2010 Program (Project CSD2007-00045) and Brazilian institution CNPq (Project 573636/2008-7 and Grant 150753/2013-6). We also acknowledge the Servei Informàtica, Universitat Jaume I, for the generous allotment of computer time.

REFERENCES

- (1) Ringwood, A. E. *Composition and Petrology of Earth's Mantle*; McGraw Hill: New York, 1975.
- (2) Weinstein, B. A.; Zallen, R. Pressure-Raman effects in covalent and molecular solids. In *Light Scattering in Solids IV*; Cardona, M., Guntherodt, G., Eds.; Topics in Applied Physics, Vol. 54; Springer: Berlin, 1984; p 463.
- (3) *Ultrahigh-Pressure Mineralogy: Physics and Chemistry of the Earth's Deep Interior*; Hemley, R. J., Ed.; Reviews in Mineralogy, Vol. 37; Mineralogical Society of America: Washington, DC, 1998.
- (4) Hemley, R. J.; Ashcroft, N. W. The Revealing Role of Pressure in the Condensed Matter Sciences. *Phys. Today* **1998**, *51*, 26–32.
- (5) Hemley, R. J. Effects of High Pressure on Molecules. *Annu. Rev. Phys. Chem.* **2000**, *51*, 763.
- (6) McMillan, P. F. New Materials from High-Pressure Experiments. *Nat. Mater.* **2002**, *1*, 19–25.
- (7) Grochala, W.; Hoffmann, R.; Feng, J.; Ashcroft, N. W. The Chemical Imagination at Work in Very Tight Places. *Angew. Chem., Int. Ed.* **2007**, *46*, 3620–3642.
- (8) Maczka, M.; Souza, A. G.; Paraguassu, W.; Freire, P. T. C.; Mendes, J.; Hanuza, J. Pressure-Induced Structural Phase Transitions and Amorphization in Selected Molybdates and Tungstates. *Prog. Mater. Sci.* **2012**, *57*, 1335–1381.
- (9) Yamasaki, Y.; Miyasaka, S.; Kaneko, Y.; He, J. P.; Arima, T.; Tokura, Y. Magnetic Reversal of the Ferroelectric Polarization in a Multiferroic Spinel Oxide. *Phys. Rev. Lett.* **2006**, *96*, No. 207204.
- (10) Zhang, X. W.; Zunger, A. Diagrammatic Separation of Different Crystal Structures of $A(2)BX(4)$ Compounds without Energy Minimization: A Pseudopotential Orbital Radii Approach. *Adv. Funct. Mater.* **2010**, *20*, 1944–1952.
- (11) Gulbinski, W.; Suszko, T. Thin Films of $\text{MoO}_3\text{-Ag}_2\text{O}$ Binary Oxides: The High Temperature Lubricants. *Wear* **2006**, *261*, 867–873.
- (12) Sanson, A.; Rocca, F.; Armellini, C.; Ahmed, S.; Grisenti, R. Local Study on the MoO_4 Units in AgI-Doped Silver Molybdate Glasses. *J. Non-Cryst. Solids* **2008**, *354*, 94–97.
- (13) Liu, E. Y.; Wang, W. Z.; Gao, Y. M.; Jia, J. H. Tribological Properties of Adaptive Ni-Based Composites with Addition of Lubricious Ag_2MoO_4 at Elevated Temperatures. *Tribol. Lett.* **2012**, *47*, 21–30.

- (14) Bhattacharya, S.; Ghosh, A. Silver Molybdate Nanoparticles, Nanowires, and Nanorods Embedded in Glass Nanocomposites. *Phys. Rev. B* **2007**, 75, No. 092103.
- (15) Cheng, L.; Shao, Q.; Shao, M. W.; Wei, X. W.; Wu, Z. C. Photoswitches of One-Dimensional Ag_2MoO_4 ($M = \text{Cr}, \text{Mo}, \text{and W}$). *J. Phys. Chem. C* **2009**, 113, 1764–1768.
- (16) Fodjo, E. K.; Li, D.-W.; Marius, N. P.; Albert, T.; Long, Y.-T. Low Temperature Synthesis and SERS Application of Silver Molybdenum Oxides. *J. Mater. Chem. A* **2013**, 1, 2558–2566.
- (17) Singh, D. P.; Sirota, B.; Talpatra, S.; Kohli, P.; Rebholz, C.; Aouadi, S. M. Broom-like and Flower-like Heterostructures of Silver Molybdate through pH Controlled Self Assembly. *J. Nanoparticle Res.* **2012**, 14, 781.
- (18) Saito, K.; Kazama, S.; Matsubara, K.; Yui, T.; Yagi, M. Monoclinic $\text{Ag}_2\text{Mo}_2\text{O}_7$ Nanowire: A New Ag-Mo-O Nanophotocatalyst Material. *Inorg. Chem.* **2013**, 52, 8297–8299.
- (19) Wyckoff, R. W. G. The Crystal Structure of Silver Molybdate. *J. Am. Chem. Soc.* **1922**, 44, 1994–1998.
- (20) Stone, D.; Liu, J.; Singh, D. P.; Muratore, C.; Voevodin, A. A.; Mishra, S.; Rebholz, C.; Ge, Q.; Aouadi, S. M. Layered Atomic Structures of Double Oxides for Low Shear Strength at High Temperatures. *Scr. Mater.* **2010**, 62, 735–738.
- (21) Gracia, L.; Beltrán, A.; Andrés, J.; Franco, R.; Recio, J. M. Quantum-Mechanical Simulation of MgAl_2O_4 under High Pressure. *Phys. Rev. B* **2002**, 66, 224114.
- (22) Gracia, L.; Beltrán, A.; Andrés, J. A Theoretical Study on the Pressure-Induced Phase Transitions in the Inverse Spinel Structure Zn_3SnO_4 . *J. Phys. Chem. C* **2011**, 115, 7740–7746.
- (23) Arora, A. K.; Nithya, R.; Misra, S.; Yagi, T. Behavior of Silver Molybdate at High-Pressure. *J. Solid State Chem.* **2012**, 196, 391–397.
- (24) Dovesi, R.; Saunders, V. R.; Roetti, C.; Orlando, R.; Zicovich-Wilson, C. M.; Pascale, F.; Civalieri, B.; Doll, K.; Harrison, N. M.; Bush, I. J.; D'Arco, P.; Llunell, M. CRYSTAL09 User's Manual; University of Torino, 2009.
- (25) Becke, A. D. Density-Functional Thermochemistry. The Role of Exact Exchange. *J. Chem. Phys.* **1993**, 98, 5648–5652.
- (26) Lee, C. T.; Yang, W. T.; Parr, R. G. Development of the Colle-Salvetti Correlation-Energy Formula into a Functional of the Electron-Density. *Phys. Rev. B* **1988**, 37, 785–789.
- (27) Blanco, M. A.; Francisco, E.; Luana, V. GIBBS: Isothermal-Isobaric Thermodynamics of Solids from Energy Curves Using a Quasi-Harmonic Debye Model. *Comput. Phys. Commun.* **2004**, 158, 57–72.
- (28) Bocharov, D.; Gryaznov, D.; Zhukovskii, Y. F.; Kotomin, E. A. Ab Initio Modeling of Oxygen Impurity Atom Incorporation into Uranium Mononitride Surface and Sub-Surface Vacancies. *J. Nucl. Mater.* **2011**, 416, 200–204.
- (29) Dorado, B.; Freyss, M.; Martin, G. GGA plus U Study of the Incorporation of Iodine in Uranium Dioxide. *Eur. Phys. J. B* **2009**, 69, 203–209.
- (30) Lee, Y. L.; Kleis, J.; Rossmeisl, J.; Morgan, D. Ab initio Energetics of $\text{LaBO}_3(001)$ ($B = \text{Mn}, \text{Fe}, \text{Co}, \text{and Ni}$) for Solid Oxide Fuel Cell Cathodes. *Phys. Rev. B* **2009**, 80, No. 224101.
- (31) Martinez, J. I.; Hansen, H. A.; Rossmeisl, J.; Norskov, J. K. Formation Energies of Rutile Metal Dioxides Using Density Functional Theory. *Phys. Rev. B* **2009**, 79, No. 045120.
- (32) Levy, D.; Pavese, A.; Hanfland, M. Synthetic MgAl_2O_4 (Spinel) at High-Pressure Conditions (0.0001–30 GPa): A Synchrotron X-Ray Powder Diffraction Study. *Am. Mineral.* **2003**, 88, 93–98.
- (33) <http://what-when-how.com/nanoscience-and-nanotechnology/mixed-metal-oxide-nanoparticles-part-2-nanotechnology/>
- (34) Stevanovic, V.; d'Avezac, M.; Zunger, A. Universal Electrostatic Origin of Cation Ordering in $A(2)BO(4)$ Spinel Oxides. *J. Am. Chem. Soc.* **2011**, 133, 11649–11654.
- (35) Seko, A.; Oba, F.; Tanaka, I. Classification of Spinel Structures Based on First-Principles Cluster Expansion Analysis. *Phys. Rev. B* **2010**, 81, No. 054114.
- (36) Seko, A.; Yuge, K.; Oba, F.; Kuwabara, A.; Tanaka, I. Prediction of Ground-State Structures and Order-Disorder Phase Transitions in II-III Spinel Oxides: A Combined Cluster-Expansion Method and First-Principles Study. *Phys. Rev. B* **2006**, 73, No. 184117.
- (37) Wenda, E. Phase Diagram of the $\text{V}_2\text{O}_5\text{-MoO}_3\text{-Ag}_2\text{O}$ System. *J. Therm. Anal. Calorim.* **1990**, 36, 1417–1427.
- (38) Wenda, E. High Temperature Reactions in the $\text{MoO}_3\text{-Ag}_2\text{O}$ System. *J. Therm. Anal. Calorim.* **1998**, 53, 861–870.
- (39) Li, Z. Q.; Chen, X. T.; Xue, Z.-L. Microwave-Assisted Hydrothermal Synthesis of Cube-like $\text{Ag-Ag}_2\text{MoO}_4$ with Visible-Light Photocatalytic Activity. *Sci. China: Chem.* **2013**, 56, 443–450.
- (40) Kim, D. W.; Cho, I. S.; Lee, S.; Bae, S. T.; Shin, S. S.; Han, G. S.; Jung, H. S.; Hong, K. S. Photophysical and Photocatalytic Properties of $\text{Ag}_2\text{M}_2\text{O}_7$ ($M = \text{Mo}, \text{W}$). *J. Am. Ceram. Soc.* **2010**, 93, 3867–3872.
- (41) Hashim, M.; Hu, C. G.; Chen, Y. X.; Zhang, C. L.; Xi, Y.; Xu, J. Synthesis, Characterization, and Optical Properties of $\text{Ag}_2\text{Mo}_2\text{O}_7$ Nanowires. *Phys. Status Solidi A* **2011**, 208, 1937–1941.
- (42) <http://www.cryst.ehu.es/cgi-bin/cryst/programs//nph-sam>